JOM, Vol. 68, No. 10, 2016
DOI: 10.1007/s11837-016-2060-5

Mg_2Si-Based Materials for the Thermoelectric Energy Conversion

X. CHENG,[1] N. FARAHI,[1] and H. KLEINKE[1,2]

1.—Department of Chemistry, Waterloo Institute for Nanotechnology, University of Waterloo, Waterloo, ON N2L 3G1, Canada. 2.—e-mail: kleinke@uwaterloo.ca

Thermoelectric materials are capable of converting a temperature gradient into electricity (thermoelectric power generation) and vice versa (Peltier cooling). The thermoelectric power generation has been used for decades in spacecraft, where radioactive decay provides the heat source. Additional applications under consideration are based on the utilization of waste heat, for example in automotives or the manufacturing industries. Commercial thermoelectric materials are normally based on Bi_2Te_3, PbTe, or possibly in the future on the so-called filled skutterudites, such as $Yb_xCo_4Sb_{12}$. The downside of these materials is that some of their major constituent elements are toxic, namely tellurium, lead, and antimony, and in part rare and expensive (ytterbium, tellurium). Mg_2Si on the other hand is composed of abundant, environmentally benign elements, and thus offers a huge advantage for commercial applications. Here, we provide a review of Mg_2Si-based materials for thermoelectric energy conversion, discussing how competitive these materials have become in comparison to the above-mentioned more traditional materials.

Key words: Thermoelectrics, energy, magnesium, silicon, tin, bismuth

INTRODUCTION

Thermoelectric Energy Conversion

Thermoelectric (TE) materials can convert a temperature gradient into electricity, utilizing the Seebeck effect, or use electricity to generate a temperature gradient, known as Peltier cooling. Peltier cooling is employed in portable coolers and laptops, as well as possibly for temperature control in car seats.[1] More than half of the energy generated by mankind is lost as waste heat, but TE materials may tap into this waste heat, otherwise lost, and convert it in part into useful energy. For several decades, space missions from *Voyager* to *Curiosity* have used the Seebeck effect[2,3] and nowadays thermoelectric generators are being tested on Earth for waste heat recovery in stationary applications as well as automotives.[4,5] The relatively low conversion efficiency, as well as the price and toxicity of these materials, still mitigate against a wider use of this technology.[6,7]

TE materials are classified based on their figure-of-merit, defined as $zT = T\alpha^2\sigma\kappa^{-1}$, with α being the Seebeck coefficient, σ the electrical conductivity, κ the thermal conductivity, and T the average temperature. Thermoelectric devices are composed of n- and p-doped semiconducting legs, which are connected electrically in series and thermally in parallel. The figure-of-merit of such a device, ZT, is a function of the zT values of the constituent materials involved. The average $\overline{ZT}$ over the applied temperature range goes directly into the formula Eq. 1 for the conversion efficiency η:

$$\eta = \frac{T_H - T_C}{T_H} \frac{\sqrt{1+\overline{ZT}} - 1}{\sqrt{1+\overline{ZT}} + \frac{T_C}{T_H}} \quad (1)$$

There T_H denotes the hot temperature and T_C the cold temperature. Larger ZT values thus lead to larger conversion efficiency. Advanced thermoelectrics are semiconductors,[8,9] so that the energy gap can prevent the co-existence of p- and n-type carriers. To obtain the best compromise of having

(Published online August 8, 2016)

both a high Seebeck coefficient α and a high electrical conductivity σ, these semiconductors are typically doped to a charge carrier concentration of the order of 10^{19} to 10^{20} cm^{-3}.[10] Furthermore, most of the advanced thermoelectrics are comprised of heavy elements, which provide a lower phonon contribution to the thermal conductivity, in turn reducing the total thermal conductivity. The latter consists of two parts, namely the lattice, κ_L, and the electronic thermal conductivity, κ_e, arising from the charge carriers, according to $\kappa = \kappa_L + \kappa_e$. Highly complex structures may also provide an advantage in reducing thermal conductivity, but this may also cause a lowered electrical conductivity through lowering the mobility of the charge carriers.[11]

Advanced Thermoelectric Materials

Traditionally, variants of Bi_2Te_3, a semiconductor with a narrow gap of 0.16 eV.[12] have been employed for applications at temperatures below 500 K. The crystal structure of Bi_2Te_3 is a layered defect variant of the NaCl type, which in turn is adopted by PbTe, a well-known high-temperature thermoelectric material with a gap of 0.32 eV.[13] Alloying with Sb afforded a maximum $zT = 1.0$ at 300 K for *p*-type Bi_2Te_3, and nanostructuring led to a performance increase as evidenced in $zT = 1.4$ at 300 K.[14] Nanowires can exhibit even better performance[15,16] for example in case of Bi_2Te_3 with zT values > 2 at 300 K.[17] Bulk *n*-type Bi_2Te_3 may also exhibit zT values in excess of unity, e.g. $zT = 1.2$ at 423 K.[18] Modifications of PbTe may exceed these zT values, for example in the *p*-type $Tl_{0.02}Pb_{0.98}Te$ with $zT = 1.5$ at 773 K,[19] in $Na_{0.02}Pb_{0.98}Se_{0.15}Te_{0.85}$ with $zT = 1.8$ at 850 K[20] in SALT materials (sodium-antimony-lead-tellurium), e.g. $Na_{0.95}Pb_{20}SbTe_{22}$ with $zT = 1.7$ at 650 K,[21] and in the LASTT materials (lead-antimony-silver-tellurium-tin) $Ag(Pb_{1-y}Sn_y)_mSbTe_{m+2}$ with nanodomains, achieving a high $zT = 1.5$ at the lower temperature of 627 K.[22] On the *n*-type side, the LAST materials (lead-antimony–silver–tellurium), e.g. $AgPb_{18}SbTe_{20}$, stand out with $zT = 2.1$ at 800 K.[23] Finally, a *p*-type composite of PbTe doped with 2% Na and embedded 4% of SrTe was reported to achieve $zT = 2.2$ at 915 K.[24]

More complex materials exhibiting comparable performance, in part because of their low thermal conductivity, are skutterudites and clathrates, including the *n*-type triple-filled skutterudite $Ba_{0.08}La_{0.05}Yb_{0.04}Co_4Sb_{12}$ with $zT = 1.7$ at 850 K[25] and the *n*-type clathrate $Ba_8Ni_{0.31}Zn_{0.52}Ga_{13.06}Ge_{32.2}$ with $zT = 1.2$ at 1000 K[26] and the best Si-based clathrate $Ba_8Ga_{16}Si_{30}$ with $zT = 0.87$ at 873 K.[27] Zintl materials[28] often adopt even more complex structures with lower thermal conductivity, with examples such as the *p*-types $Ni_{0.06}Mo_3Sb_{5.4}Te_{1.6}$ with $zT = 0.93$ at 1050 K,[29] $Sr_3Ga_{1-x}Zn_xSb_3$ with $zT = 0.97$ at 1000 K,[30] $La_{0.4}Yb_{13.6}MnSb_{11}$ with $zT = 1.15$ at 1150 K,[31] $Yb_{14}Mn_{0.4}Al_{0.6}Sb_{11}$ with $zT = 1.32$ at 1275 K[32] and β-Zn_4Sb_3 with $zT = 1.3$ at 670 K.[33]

Among the materials with low lattice thermal conductivity of $\kappa_L < 1$ W m^{-1} K^{-1}, thallium tellurides stand out with values often below 0.5 W m^{-1} K^{-1}.[34] This has led to several Tl tellurides exhibiting zT values above unity (at intermediate temperatures) as well, including values of 1.1 for $Tl_9Bi_{0.98}Te_6$ at 500 K,[35] 1.2 for $TlAg_9Te_5$ at 700 K,[36] 1.2 for zone-refined Tl_9BiTe_6 at 500 K[37] and finally 1.3 for $Tl_{8.05}Sn_{1.95}Te_6$ and 1.5 for $Tl_{8.10}Pb_{1.90}Te_6$ at 680 K.[38]

Most of the materials discussed above are antimonides and tellurides, and therefore toxicity is a major concern. On top of that, several metals occur in these materials that are of comparable or even higher toxicity, most notably thallium and lead. Affordability is another important issue for commercial applications of these materials, as some of these elements are rare and/or expensive, namely tellurium, ytterbium and silver. While cations from Tl to Bi and anions from Sb to Te are natural choices to form heavy materials exhibiting low thermal conductivity, the performance of Mg_2Si-based materials demonstrates that lighter elements may also be employed as advanced thermoelectrics.[39] Details of their thermoelectric properties are presented in the current review in comparison with established state-of-the-art materials.

RESULTS AND DISCUSSION

Synthesis of Mg_2Si-Based Materials

The synthesis of Mg_2Si is challenging for a number of reasons, namely the high affinity of magnesium for oxygen, the high vapor pressure of Mg, the high melting temperature of silicon at 1687 K, and the almost identical melting point of Mg_2Si at 1358 K and boiling point of Mg at 1363 K. As a consequence, many Mg_2Si samples exhibit MgO impurities.[40] Therefore, several different methods in addition to classical ceramic methods have been devised, including the vertical Bridgman method using molten Mg_2Si,[41] crystal growth from molten $Mg_2Si_{1-x}Ge_x$,[42] B_2O_3 flux method,[43] microwave assisted fast synthesis after ball-milling,[44] vacuum plasma spray,[45] a solid-state metathesis reaction of NaSi, $MgCl_2$ and Na,[46] and liquid encapsulated vertical gradient freezing using a $KCl/MgCl_2$ eutectic mixture as encapsulant.[47] Recently, an "ultrafast self-propagating high-temperature synthesis" was developed in which a cylinder of Mg, Si and Sb reacted after ignition within seconds in air to yield Sb-doped Mg_2Si.[48] The same authors also prepared other thermoelectrics via this method.[49] In several of these methods, an excess of magnesium was used to compensate for its vapor loss.

Crystal Structure and Semiconducting Properties of Mg_2Si

Mg_2Si crystallizes in the antifluorite type, also adopted by Mg_2C, Mg_2Ge, Mg_2Sn, and Mg_2Pb.[50] The Si atoms form a face-centered cubic lattice, in which all tetrahedral holes are filled by Mg atoms (Fig. 1). Additional Mg atoms may also occupy some of the octahedral holes,[51] which changes the electron count and thus the charge carrier concentration.[52] Mg_2C is a high-pressure phase[53] and Mg_2Pb a semimetal,[50,54] while Mg_2Si, Mg_2Ge, and Mg_2Sn are semiconductors with experimentally determined band gaps of 0.77, 0.74 and 0.36 eV, respectively, i.e. decreasing gaps from the silicide to the stannide.[55]

With such a band gap, the intrinsic carrier concentration of Mg_2Si is very low, resulting in a low electrical conductivity of undoped Mg_2Si of only $\sigma = 3\ \Omega^{-1}\ cm^{-1}$ around room temperature (RT).[56] Because of the light constituent elements and the small high symmetry unit cell, the lattice thermal conductivity is of the order of $\kappa = 10\ W\ m^{-1}\ K^{-1}$ at RT, which needs to be decreased, in addition to increasing the charge carrier concentration, before Mg_2Si can be considered for the thermoelectric energy conversion.

Thermoelectric Properties of Bulk Mg_2Si-Based Materials

Substituting Si in part with Ge or Sn atoms aids in reducing the thermal conductivity, because of the enhanced mass fluctuation combined with an overall increased molar mass.[57] For example, using 30% Ge on the Si site, we obtained less than $3\ W\ m^{-1}\ K^{-1}$ at RT[58] compared to about $10\ W\ m^{-1}\ K^{-1}$[56] for Mg_2Si. A problem with using tin stems from the reported miscibility gap, in contrast to the complete solid solution of $Mg_2Si_{1-x}Ge_x$. Depending on the synthesis method,[59] the miscibility gap may occur between 40% and 60% Sn on the Si site.[60] This problem may be overcome by optimizing the synthesis conditions, e.g. by using a B_2O_3 flux (preparing Sb-doped $Mg_2Si_{0.5}Sn_{0.5}$).[43] In 2015, a low thermal conductivity of $\kappa = 1.9\ W\ m^{-1}\ K^{-1}$ at 300 K was reported for a sample of nominal composition $Mg_2Si_{0.5}Sn_{0.5}$ prepared from Mg_2Si and Mg_2Sn, but this sample inadvertently contained MgO nanoparticles as well as traces of unreacted Si and Sn that may have contributed to this low value.[61] With values between 2 and 3 $W\ m^{-1}\ K^{-1}$ at RT, the lattice thermal conductivity begins to be competitive with other thermoelectrics such as PbTe, while still being higher than that of Bi_2Te_3, the filled skutterudites or various clathrates.

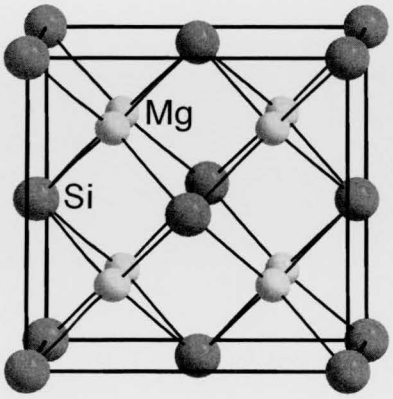

Fig. 1. Crystal structure of Mg_2Si. Small circles Mg; large circles Si.

The most widely used *n*-type doping elements here are antimony and bismuth, shown to substitute for the Si atoms.[62] These elements belong to group 15 of the periodic table, and thus contribute one extra electron for each replaced Si atom from group 14. Because of the larger size of the Sb and Bi atoms, compared to Si, the amount of Sb and Bi is limited to less than 3% on the Si site.[63] This amount may be increased in case of the alloyed samples $Mg_2Si_{1-x}Ge_x$ and $Mg_2Si_{1-x}Sn_x$, likely because of their unit cell expansions stemming from the larger sizes of Ge and Sn in comparison to Si atoms.[64] Each percent of Sb or Bi corresponds to an expected increase in the carrier concentration of $1.6 \times 10^{20}\ cm^{-3}$, but most often smaller increases were found, possibly because of the formation of Mg_3Sb_2 or Mg_3Bi_2 in the grain boundaries. For example, we found $n = 3.5 \times 10^{19}$ electrons per cm^3 and 9.5×10^{19} electrons per cm^3 for the hot-pressed materials of nominal composition $Mg_2Si_{0.98}Sb_{0.02}$ and $Mg_2Si_{0.98}Bi_{0.02}$, respectively, instead of the $3.1 \times 10^{20}\ cm^{-3}$ calculated based on the formulae.[62] Similarly, Zhang et al.[65] reported $n = 8.6 \times 10^{19}$ electrons per cm^3 for $Mg_2Si_{0.4}Sn_{0.6}Bi_{0.02}$ and $n = 2.9 \times 10^{20}$ electrons per cm^3 for $Mg_2Si_{0.4}Sn_{0.6}Bi_{0.03}$, prepared by melt-spinning and consolidated by spark-plasma-sintering (MS-SPS). Depending on the synthesis technique, the density and doping level, electrical conductivity values of Sb- and Bi-doped samples typically range from $\sigma = 400\ \Omega^{-1}\ cm^{-1}$[58] to $2000\ \Omega^{-1}\ cm^{-1}$ in the case of $Mg_{2.16}(Si_{0.4}Sn_{0.6})_{0.97}Bi_{0.03}$ with a carrier concentration of $2.4 \times 10^{20}\ cm^{-3}$ at RT,[66] and then decrease with increasing temperature.

The thermal and electrical conductivity of selected high performance Sb- and Bi-doped Mg_2Si-based bulk materials are compared in Fig. 2a and b, respectively, all of them exhibiting zT_{max} values in excess of unity. Three of these samples were synthesized via solid state reactions, followed by spark-plasma-sintering, namely $Mg_{2.20}Si_{0.49}Sn_{0.5}Sb_{0.01}$,[67] $Mg_{2.16}(Si_{0.4}Sn_{0.6})_{0.985}Sb_{0.015}$,[68] and $Mg_{2.16}(Si_{0.4}Sn_{0.6})_{0.97}Bi_{0.03}$ pressed via SPS.[66] In addition, an Sb-doped $Mg_2Si_{0.5}Sn_{0.5}$ material with a high porosity of 37%, consolidated via pressureless SPS,[69] and $Mg_2Si_{0.4}Sn_{0.6}Bi_{0.03}$, prepared via melt-spinning, followed by spark-plasma-sintering (MS-SPS)[65] are shown in Fig. 2. The melt-spinning method resulted in the formation of nanoscale precipitates with sizes of 10–20 nm, while $Mg_{2.16}(Si_{0.4}Sn_{0.6})_{0.985}Sb_{0.015}$ contained a Sn-rich phase with particle sizes of 20–30 nm, deduced to stem from that composition being

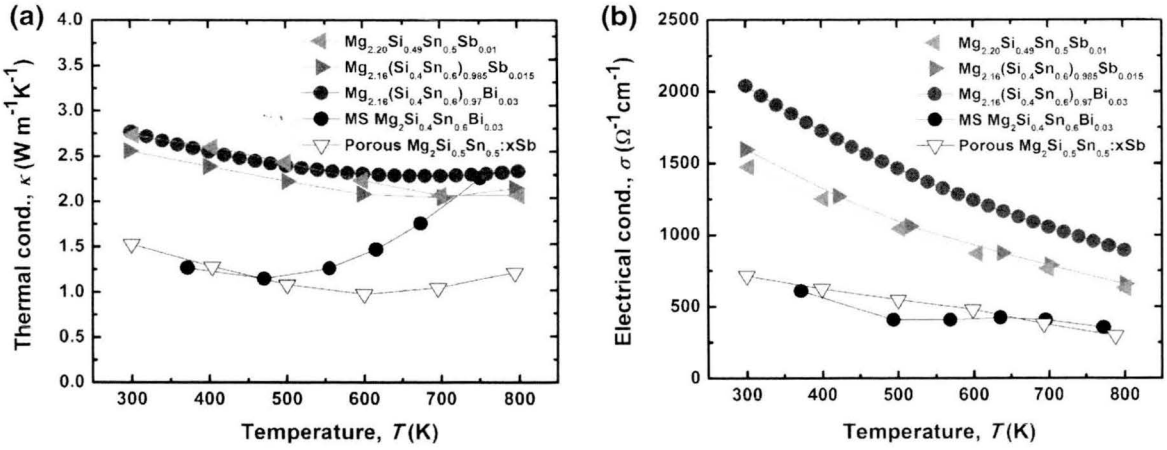

Fig. 2. (a) Thermal conductivity and (b) electrical conductivity of various high-performance materials.

close to the above-mentioned miscibility gap. These naturally occurring nanostructures are known to reduce the lattice thermal conductivity in these materials since at least 2008, as demonstrated for the series $Mg_2Si_{0.4-x}Sn_{0.6}Sb_x$.[70]

The two samples prepared via MS-SPS (labeled MS in Fig. 2) and pressureless SPS (labeled Porous) exhibit significantly lower thermal and electrical conductivity below 600 K. An upturn is observed in the thermal conductivity in both of these samples beginning between 500 K and 600 K, likely caused by the bipolar effect. The other three samples, synthesized by solid-state reactions and consolidated by SPS, now show a clear bipolar effect until 700 K; at least until then, both the thermal and the electrical conductivity decrease steadily with increasing temperature. Around RT, κ ranges from 2.56 W m^{-1} K^{-1} to 2.77 W m^{-1} K^{-1} for the regular solid-state samples, compared to 1.53 W m^{-1} K^{-1} for the porous sample, and possibly less (extrapolated) for the MS sample. Similarly, the electrical conductivity of the solid state samples varies from σ = 1470 Ω^{-1} cm^{-1} to 2040 Ω^{-1} cm^{-1}, compared to 715 Ω^{-1} cm^{-1} for the porous sample around RT. The highest conductivity occurs in the sample with the highest dopant concentration of the three, namely 3% Bi versus 1% and 1.5% Sb on the Si/Sn site. Utilizing the Wiedemann–Franz law, $\kappa_e = L\sigma T$ with L representing the Lorenz number, one can estimate the electronic contribution to the thermal conductivity, and then derive the lattice part via $\kappa_L = \kappa - \kappa_e$. The three solid-state materials exhibit very comparable lattice thermal conductivity, namely from κ_L = 1.65 W m^{-1} K^{-1} to 1.92 W m^{-1} K^{-1} at RT, while the porous sample is significantly below that, with κ_L = 1.16 W m^{-1} K^{-1}. These values compare nicely with Bi_2Te_3.

As illustrated in Fig. 3a for the same (n-type) materials shown in Fig. 2, the Seebeck coefficient α typically increases linearly with increasing temperature. Notable exceptions are the porous material and the one prepared via melt-spinning, whose Seebeck coefficient peaks around 600 K; the authors relate this to the beginning of the bipolar effect at 600 K. α may cover a large range, again depending on the doping level, and of course the temperature. The three solid-state samples exhibit very similar values and temperature dependence of the Seebeck coefficient, ranging from -120 μV K^{-1} to -132 μV K^{-1} at RT and from -217 μV K^{-1} to -230 μV K^{-1} around 800 K. Other examples include $Mg_2Si_{0.98}Bi_{0.02}$ with $\alpha = -94$ μV K^{-1} [62] and $Mg_2Si_{0.677}Ge_{0.3}Bi_{0.023}$ with -100 μV K^{-1} at RT.[58] It is not a coincidence that the Sn-containing samples often exhibit higher Seebeck values despite their larger carrier concentration (and electrical conductivity). This is caused by a convergence of the two lowest lying conduction bands, resulting in an increased valley degeneracy and thus an enhanced Seebeck coefficient, calculated to occur around 65% Sn on the Si site.[68] In addition, the porous Sb-doped $Mg_2Si_{0.5}Sn_{0.5}$ exhibits a further enhanced Seebeck coefficient with $\alpha = -154$ μV K^{-1} at RT, which was attributed to the band structure being modified by its unique microstructure.[69]

Therefore, the Sn-containing samples are the ones with the highest power factor, $P.F. = \alpha^2\sigma$. Because α increases with increasing temperature, and $P.F.$ is proportional to α^2, $P.F.$ continues to increase with increasing temperature despite the parallel decrease of σ. In the case of $Mg_{2.16}(Si_{0.4}Sn_{0.6})_{0.97}Bi_{0.03}$, the power factor changes from 30 μW cm^{-1} K^{-2} at 300 K to 42 μW cm^{-1} K^{-2} at 800 K. These numbers are highly competitive, as evident from a comparison with established thermoelectrics. The above-mentioned filled skutterudites $Ba_{0.08}La_{0.05}Yb_{0.04}Co_4Sb_{12}$ (zT_{max} = 1.7) exhibits a maximum power factor of 52 μW cm^{-1} K^{-2} [25] and the clathrate $Ba_8Ni_{0.31}Zn_{0.52}Ga_{13.06}Ge_{32.2}$ (zT_{max} = 1.2) a maximum $P.F.$ = 15 μW cm^{-1} K^{-2}.[26] Similarly, Tl-doped PbTe with zT_{max} = 1.5 has a maximum $P.F.$ = 19 μW cm^{-1} K^{-2}.[19]

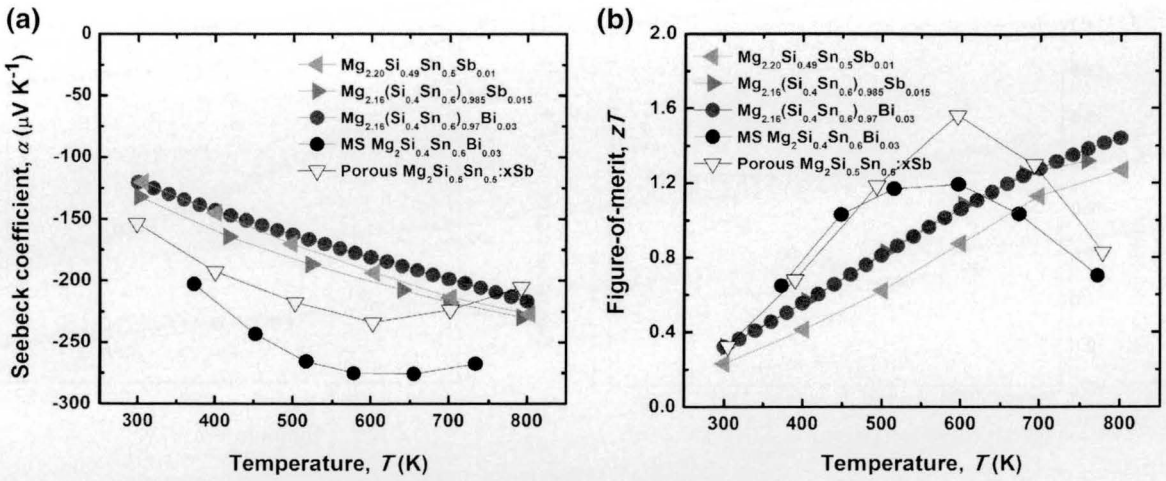

Fig. 3. (a) Seebeck coefficient and (b) figure-of-merit of various high-performance materials.

The figure-of-merit values zT, depicted in Fig. 3b, are too low for applications at ambient temperatures, all being below 0.4 around RT. On the other hand, the steady increase of zT until 600–800 K or beyond, lead to competitive performance at those temperatures, with several examples surpassing zT of unity. The first examples with $zT_{max} = 1.4$ at 800 K were published in this decade, beginning with $Mg_{2.16}(Si_{0.4}Sn_{0.6})_{0.97}Bi_{0.03}$ as shown in Fig. 3b,[66] and also including the Ge-containing $Mg_2Si_{0.53}Sn_{0.4}Ge_{0.05}Bi_{0.02}$.[71] Thus far, the highest value, $zT_{max} = 1.63$ at 615 K, was achieved by the porous Sb-doped $Mg_2Si_{0.5}Sn_{0.5}$ consolidated via pressureless SPS, also shown in Fig. 3b.[69] However, a problem with its porosity of 37% may lie in its applicability, i.e. the formation of a robust device.

No comparable *p*-type Mg_2Si materials have been identified to date. The best examples exhibit figure-of-merit values between 0.3 and 0.7, including $Mg_{2.10}(Si_{0.3}Sn_{0.7})_{0.95}Ga_{0.05}$ with $zT_{max} = 0.35$ at 650 K,[72] $Mg_2Si_{0.6}Ge_{0.4}$:Ga(0.8%) with $zT_{max} = 0.36$ at 625 K,[73] and $Mg_{1.86}Li_{0.14}Si_{0.3}Sn_{0.7}$ with $zT_{max} = 0.5$ at 750 K, where Li atoms were substituted onto the Mg site.[74] Most recently, $Mg_{1.86}Li_{0.14}Si_{0.4}Sn_{0.6}$ was prepared via melt-spinning and spark-plasma-sintering within 1 h, resulting in $zT_{max} = 0.58$ at 760 K,[75] and $Mg_2Li_{0.025}Si_{0.4}Sn_{0.6}$ was synthesized under a layer of B_2O_3, yielding $zT_{max} = 0.7$ at 675 K.[76] Comparable or even better performance may be observed in *p*-type manganese silicides, namely in $MnSi_{1.75}$ and variants thereof. This strongly depends on the preparation methods, as a comparison of the binary Mn silicides reveals that $MnSi_{1.72}$, prepared via furnace melting and SPS, exhibits $zT_{max} = 0.63$ at 723 K,[77] $MnSi_{1.75}$ (Mn_4Si_7), synthesized via induction melting and SPS, shows $zT_{max} = 0.62$ at 800 K,[78] $MnSi_{1.84}$, prepared via ball-milling and pulse discharge sintering, a $zT_{max} = 0.83$ at 818 K,[79] and $MnSi_{1.85}$, obtained via ball-milling and SPS, a $zT_{max} = 0.67$ at 873 K.[80]

Thermoelectric Properties of Bulk Mg_2Si-Based Nanocomposites

Forming nanocomposites is a proven strategy to further enhance thermoelectric materials. Ideally, this occurs with a reduction of the thermal conductivity by enhanced scattering of mid- to long-wavelength phonons, a less affected electrical conductivity and an increased Seebeck coefficient via energy filtering of the charge carriers.[81–83] Since 2012, composites of Bi-doped Mg_2Si with single-walled carbon nanohorns (SWCNH)[84] and with Si nanoparticles,[85] Bi-doped $Mg_2(Si,Ge)$ with multi-walled carbon nanotubes (MWCNT),[86] and As- and Sb-co-doped $Mg_2(Si,Sn)$ with TiO_2[87] have been investigated. While adding these nanoparticles to Mg_2Si reduced the thermal conductivity, e.g. down to 6 W m^{-1} K^{-1} at RT in the case of the Si additions, these reductions cannot match the above-discussed $Mg_2(Si,Ge)$ and $Mg_2(Si,Sn)$ solid solutions.

The nanocomposites of the solid solutions with Ge and Sn may be more relevant, as their bulk materials perform better than binary Mg_2Si. Furthermore, their thermal conductivity is already reduced, so a further reduction via nanostructuring may be more intriguing if successful. The addition of 5 vol.% insulating TiO_2 to $Mg_2(Si_{0.392}Sn_{0.6})_{0.9925}As_{0.008}Sb_{0.0075}$ led to both lower thermal and electrical conductivity, namely from $\kappa = 3.85$ W m^{-1} K^{-1} to $\kappa = 3.02$ W m^{-1} K^{-1}, and from $\sigma = 1815$ Ω^{-1} cm^{-1} to $\sigma = 1550$ Ω^{-1} cm^{-1}, respectively, at RT. On the other hand, adding MWCNT to $Mg_2Si_{0.877}Ge_{0.1}Bi_{0.023}$ lowered only the thermal conductivity (more so with increasing MWCNT concentration),[86] not the electrical conductivity (Fig. 4). This correlates well with the measured charge carrier concentration (at RT), which decreased from 1.8×10^{20} cm^{-3} to 1.3×10^{20} cm^{-3} after adding 5 vol.% TiO_2, but varied only insignificantly after adding 0.5 wt.% MWCNT, namely from to 7.1×10^{19} cm^{-3} to 7.6×10^{19} cm^{-3}.

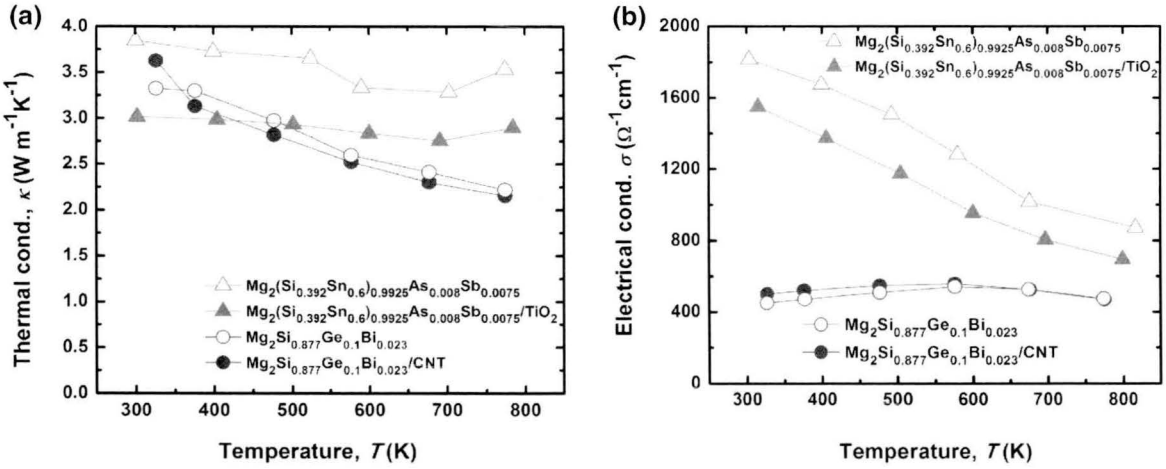

Fig. 4. (a) Thermal conductivity and (b) electrical conductivity of selected nanocomposites.

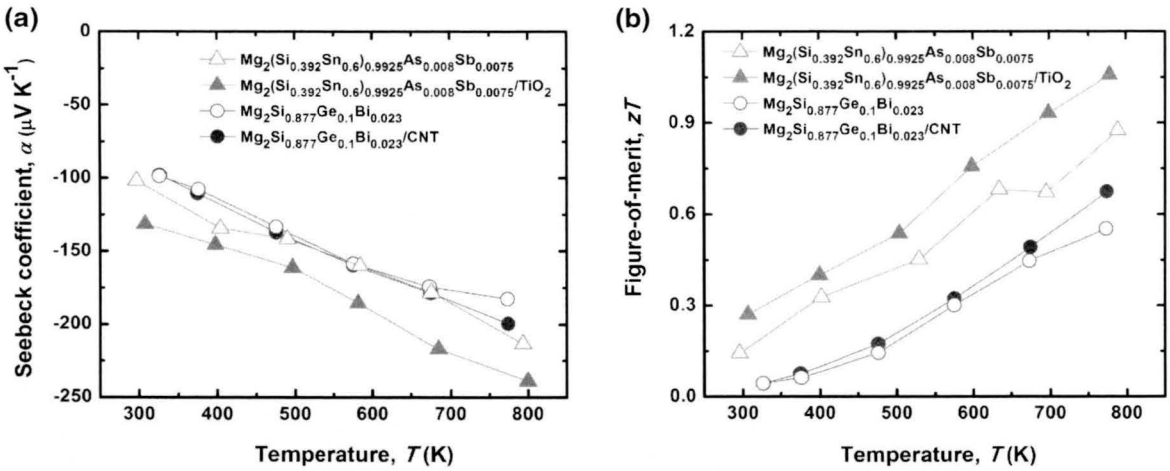

Fig. 5. (a) Seebeck coefficient and (b) figure-of-merit of selected nanocomposites.

In both cases, the Seebeck coefficient was enhanced after adding the respective nanoparticles, in particular at the higher temperatures (Fig. 5a). At 800 K, α increased from $-100\ \mu V\ K^{-1}$ to $-130\ \mu V\ K^{-1}$ in the case of 5 vol.% TiO_2. Similarly, α increased from $-183\ \mu V\ K^{-1}$ to $-200\ \mu V\ K^{-1}$ in case of 0.5 wt.% MWCNT at 773 K. These numbers result in zT_{max} enhancements from 0.9 to 1.1 and from 0.55 to 0.67, respectively (Fig. 5b).

The fact that the additions of MWCNT to $Mg_2Si_{0.877}Ge_{0.1}Bi_{0.023}$ and of TiO_2 to $Mg_2(Si_{0.392}Sn_{0.6})_{0.9925}As_{0.008}Sb_{0.0075}$ both caused an increase in zT_{max} by approximately 20%, demonstrates that this concept may also be applied to other solid solutions of Mg_2Si with Mg_2Ge and Mg_2Sn, most interestingly to the materials with the best performance to date.

CONCLUSION

Within this review, we have demonstrated that several methods exist to render Mg_2Si competitive with the best thermoelectrics at temperatures between 500 K and 800 K. Most importantly, alloying with Sn and doping with Sb and Bi, both on the Si site, followed by spark-plasma sintering, yielded several different bulk materials with naturally occurring nanoparticles, that exhibit zT values between 1.0 and 1.4 around 800 K. In addition, pressureless spark-plasma sintering afforded a porous material with enhanced Seebeck coefficient and reduced thermal conductivity, providing for the record $zT = 1.6$ at 615 K to date in this system. These performances are only surpassed by few triple-filled skutterudites and PbTe modifications with nanodomains or nano-additions, exhibiting bulk zT values between 1.7 and 2.2 at similar temperatures as presented in the "Introduction".

In addition, the Mg_2Si materials may further be enhanced via nanocomposites: first attempts yielded improvements of the order of 20% in the figure-of-merit, but were not performed on the best materials in this family. Considering all these findings occurred recently in the current decade, further improvements can be anticipated. This is particularly exciting

because of the sustainability of these materials in contrast to the toxic antimonides and tellurides. Therefore, variants of environmentally benign Mg_2Si may become the next generation materials.

ACKNOWLEDGEMENTS

Financial support from the Natural Sciences and Engineering Research Council is highly appreciated.

REFERENCES

1. H.-S. Choi, S. Yun, and K. Whang, *Appl. Therm. Eng.* 27, 2841 (2007).
2. R.R. Furlong and E.J. Wahlquist, *Nucl. News* 42, 26 (1999).
3. J. Yang and T. Caillat, *MRS Bull.* 31, 224 (2006).
4. L.E. Bell, *Science* 321, 1457 (2008).
5. M. Matsumoto, M. Mori, T. Haraguchi, M. Ohtani, T. Kubo, K. Matsumoto, and H. Matsuda, *SAE Int. J. Eng.* 8, 1815 (2015).
6. D.M. Rowe, *Thermoelectrics Handbook: Macro to Nano* (Boca Raton: CRC Press, Taylor & Francis Group, 2006).
7. M. Zebarjadi, K. Esfarjani, M.S. Dresselhaus, Z.F. Ren, and G. Chen, *Energy Environ. Sci.* 5, 5147 (2012).
8. J.O. Sofo and G.D. Mahan, *Phys. Rev. B* 49, 4565 (1994).
9. H. Kleinke, *Chem. Mater.* 22, 604 (2010).
10. G.J. Snyder and E.S. Toberer, *Nat. Mater.* 7, 105 (2008).
11. E.S. Toberer, A.F. May, and G.J. Snyder, *Chem. Mater.* 22, 624 (2010).
12. T.C. Harman, B. Paris, S.E. Miller, and H.L. Goering, *J. Phys. Chem. Solids* 2, 181 (1957).
13. Y. Gelbstein, Z. Dashevsky, and M.P. Dariel, *Phys. B* 363, 196 (2005).
14. W. Xie, S. Wang, S. Zhu, J. He, X. Tang, Q. Zhang, and T.M. Tritt, *J. Mater. Sci.* 48, 2745 (2013).
15. A.I. Hochbaum, R. Chen, R.D. Delgado, W. Liang, E.C. Garnett, M. Najarian, A. Majumdar, and P. Yang, *Nature* 451, 163 (2008).
16. A.I. Boukai, Y. Bunimovich, J. Tahir-Kheli, J.-K. Yu, W.A. Goddard III, and J.R. Heath, *Nature* 451, 168 (2008).
17. H.Y. Lv, H.J. Liu, J. Shi, X.F. Tang, and C. Uher, *J. Mater. Chem. A* 1, 6831 (2013).
18. F. Wu, H. Song, F. Gao, W. Shi, J. Jia, and X. Hu, *J. Electron. Mater.* 42, 1140 (2013).
19. J.P. Heremans, V. Jovovic, E.S. Toberer, A. Saramat, K. Kurosaki, A. Charoenphakdee, S. Yamanaka, and G.J. Snyder, *Science* 321, 554 (2008).
20. Y. Pei, X. Shi, A. LaLonde, H. Wang, L. Chen, and G.J. Snyder, *Nature* 473, 66 (2011).
21. P.F.P. Poudeu, J. D'Angelo, A.D. Downey, J.L. Short, T.P. Hogan, and M.G. Kanatzidis, *Angew. Chem. Int. Ed.* 45, 3835 (2006).
22. J. Androulakis, K.F. Hsu, R. Pcionek, H. Kong, C. Uher, J.J. D'Angelo, A. Downey, T. Hogan, and M.G. Kanatzidis, *Adv. Mater.* 18, 1170 (2006).
23. K.F. Hsu, S. Loo, F. Guo, W. Chen, J.S. Dyck, C. Uher, T. Hogan, E.K. Polychroniadis, and M.G. Kanatzidis, *Science* 303, 818 (2004).
24. K. Biswas, J. He, I.D. Blum, C.-I. Wu, T.P. Hogan, D.N. Seidman, V.P. Dravid, and M.G. Kanatzidis, *Nature* 489, 414 (2012).
25. X. Shi, J. Yang, J.R. Salvador, M. Chi, J.Y. Cho, H. Wang, S. Bai, J. Yang, W. Zhang, and L. Chen, *J. Am. Chem. Soc.* 133, 7837 (2011).
26. X. Shi, J. Yang, S. Bai, J. Yang, H. Wang, M. Chi, J.R. Salvador, W. Zhang, L. Chen, and W. Wong-Ng, *Adv. Funct. Mater.* 20, 755 (2010).
27. V.L. Kuznetsov, L.A. Kuznetsova, A.E. Kaliazin, and D.M. Rowe, *J. Appl. Phys.* 87, 7871 (2000).
28. R. Nesper, *Prog. Solid State Chem.* 20, 1 (1990).
29. H. Xu, K.M. Kleinke, T. Holgate, H. Zhang, Z. Su, T.M. Tritt, and H. Kleinke, *J. Appl. Phys.* 105, 053703 (2009).
30. A. Zevalkink, W.G. Zeier, G. Pomrehn, E. Schechtel, W. Tremel, and G.J. Snyder, *Energy Environ. Sci.* 5, 9121 (2012).
31. E.S. Toberer, S.R. Brown, T. Ikeda, S.M. Kauzlarich, and G.J. Snyder, *Appl. Phys. Lett.* 93, 062110 (2008).
32. E.S. Toberer, C.A. Cox, S.R. Brown, T. Ikeda, A.F. May, S.M. Kauzlarich, and G.J. Snyder, *Adv. Funct. Mater.* 18, 2795 (2008).
33. T. Caillat, J.-P. Fleurial, and A. Borshchevsky, *J. Phys. Chem. Solids* 58, 1119 (1997).
34. K. Kurosaki and S. Yamanaka, *Phys. Status Solidi* 210, 82 (2013).
35. Q. Guo, M. Chan, B.A. Kuropatwa, and H. Kleinke, *Chem. Mater.* 25, 4097 (2013).
36. K. Kurosaki, A. Kosuga, H. Muta, M. Uno, and S. Yamanaka, *Appl. Phys. Lett.* 87, 061919 (2005).
37. B. Wölfing, C. Kloc, J. Teubner, and E. Bucher, *Phys. Rev. Lett.* 86, 4350 (2001).
38. Q. Guo, A. Assoud, and H. Kleinke, *Adv. Energy Mater.* 4, 1400348 (2014).
39. S. LeBlanc, S.K. Yee, M.L. Scullin, C. Dames, and K.E. Goodson, *Renew. Sustain. Energy Rev.* 32, 313 (2014).
40. T. Ikeda, L. Haviez, Y. Li, and G.J. Snyder, *Small* 8, 2350 (2012).
41. M. Yoshinaga, T. Iida, M. Noda, T. Endo, and Y. Takanashi, *Thin Solid Films* 461, 86 (2004).
42. Y. Maeda, K.P. Homewood, T. Sadoh, Y. Terai, K. Yamaguchi, K. Akiyama, M. Akasaka, T. Iida, K. Nishio, and Y. Takanashi, *Thin Solid Films* 515, 8237 (2007).
43. H. Gao, T. Zhu, X. Liu, L. Chen, and X. Zhao, *J. Mater. Chem.* 21, 5933 (2011).
44. D. Berthebaud and F. Gascoin, *J. Solid State Chem.* 202, 61 (2013).
45. G. Fu, L. Zuo, J. Longtin, C. Nie, and R. Gambino, *J. Appl. Phys.* 114, 144905 (2013).
46. H. Itahara, T. Yamada, S.-Y. Oh, R. Asahi, H. Imagawa, and H. Yamane, *Chem. Commun.* 50, 4315 (2014).
47. R. Nakagawa, H. Katsumata, S. Hashimoto, and S. Sakuragi, *Jpn. J. Appl. Phys.* 54, 085503 (2015).
48. Q. Zhang, X. Su, Y. Yan, H. Xie, T. Liang, Y. You, X. Tang, and C. Uher, *ACS Appl. Mater. Interfaces* 8, 3268 (2016).
49. X. Su, F. Fu, Y. Yan, G. Zheng, T. Liang, Q. Zhang, X. Cheng, D. Yang, H. Chi, X. Tang, Q. Zhang, and C. Uher, *Nat. Commun.* 5, 4908 (2014).
50. D. Wood and A. Zunger, *Phys. Rev. B* 34, 4105 (1986).
51. M. Kubouchi, K. Hayashi, and Y. Miyazaki, *J. Alloys Compd.* 617, 389 (2014).
52. Z. Du, T. Zhu, Y. Chen, J. He, H. Gao, G. Jiang, T.M. Tritt, and X. Zhao, *J. Mater. Chem.* 22, 6838 (2012).
53. O.O. Kurakevych, T.A. Strobel, D.Y. Kim, and G.D. Cody, *Angew. Chem. Int. Ed.* 52, 8930 (2013).
54. O. Madelung, U. Rössler, M. Schulz (eds.), *Non-Tetrahedrally Bonded Elements and Binary Compounds I, Landolt-Börnstein—Group III Condensed Matter*, Vol. 41C (Berlin: Springer, 1998).
55. U. Winkler, *Helv. Phys. Acta* 28, 633 (1955).
56. D. Cederkrantz, N. Farahi, K.A. Borup, B.B. Iversen, M. Nygren, and A.E.C. Palmqvist, *J. Appl. Phys.* 111, 023701 (2012).
57. V.K. Zaitsev, M.I. Fedorov, E.A. Gurieva, I.S. Eremin, P.P. Konstantinov, A.Y. Samunin, and M.V. Vedernikov, *Phys. Rev. B* 74, 045207 (2006).
58. N. Farahi, S. Prabhudev, G. Botton, J. Zhao, J.S. Tse, Z. Liu, J.R. Salvador, and H. Kleinke, *J. Alloys Compd.* 644, 249 (2015).
59. L. Chen, G. Jiang, Y. Chen, Z. Du, X. Zhao, T. Zhu, J. He, and T.M. Tritt, *J. Mater. Res.* 26, 3038 (2011).
60. E.N. Nikitin, V.G. Bazanov, and V.I. Tarasov, *Sov. Phys. Solid State* 3, 2648 (1961).
61. J.-W. Liu, M. Song, M. Takeguchi, N. Tsujii, and Y. Isoda, *J. Electron. Mater.* 44, 407 (2015).
62. N. Farahi, M. VanZant, J. Zhao, J.S. Tse, S. Prabhudev, G. Botton, J.R. Salvador, F. Borondics, Z. Liu, and H. Kleinke, *Dalton Trans.* 43, 14983 (2014).

63. A. Kolezynski, P. Nieroda, P. Jelen, M. Sitarz, and K.T. Wojciechowski, *Vib. Spectrosc.* 76, 31 (2015).
64. S.K. Bux, M.T. Yeung, E.S. Toberer, G.J. Snyder, R.B. Kaner, and J.-P. Fleurial, *J. Mater. Chem.* 21, 12259 (2011).
65. X. Zhang, H. Liu, Q. Lu, J. Zhang, and F. Zhang, *Appl. Phys. Lett.* 103, 063901 (2013).
66. W. Liu, Q. Zhang, K. Yin, H. Chi, X. Zhou, X. Tang, and C. Uher, *J. Solid State Chem.* 203, 333 (2013).
67. W. Liu, X. Tang, H. Li, and J. Sharp, *Chem. Mater.* 23, 5256 (2011).
68. W. Liu, X. Tan, K. Yin, H. Liu, X. Tang, J. Shi, Q. Zhang, and C. Uher, *Phys. Rev. Lett.* 108, 166601 (2012).
69. H. Ning, G.D. Mastrorillo, S. Grasso, B. Du, T. Mori, C. Hu, Y. Xu, K. Simpson, G. Maizza, and M. Reece, *J. Mater. Chem. A* 3, 17426 (2015).
70. Q. Zhang, J. He, T.J. Zhu, S.N. Zhang, X.B. Zhao, and T.M. Tritt, *Appl. Phys. Lett.* 93, 102109 (2008).
71. A.U. Khan, N. Vlachos, and T. Kyratsi, *Scr. Mater.* 69, 606 (2013).
72. W. Liu, K. Yin, X. Su, H. Li, Y. Yan, X. Tang, and C. Uher, *Intermetallics* 32, 352 (2013).
73. H. Ihou-Mouko, C. Mercier, J. Tobola, G. Pont, and H. Scherrer, *J. Alloys Compd.* 509, 6503 (2011).
74. Q. Zhang, L. Cheng, W. Liu, Y. Zheng, X. Su, H. Chi, H. Liu, Y. Yan, X. Tang, and C. Uher, *Phys. Chem. Chem. Phys.* 16, 23576 (2014).
75. X. Tang, G. Wang, Y. Zheng, Y. Zhang, K. Peng, L. Guo, S. Wang, M. Zeng, J. Dai, G. Wang, and X. Zhou, *Scr. Mater.* 115, 52 (2016).
76. P. Gao, J.D. Davis, V.V. Poltavets, and T.P. Hogan, *J. Mater. Chem. C* 4, 929 (2016).
77. Y. Sadia and Y. Gelbstein, *J. Electron. Mater.* 41, 1504 (2012).
78. W. Luo, H. Li, Y. Yan, Z. Lin, X. Tang, Q. Zhang, and C. Uher, *Intermetallics* 19, 404 (2011).
79. M. Yoshikura and T. Itoh, *J. Jpn. Soc. Powder Powder Metall.* 57, 242 (2010).
80. M. Umemoto, Z.G. Liu, R. Omatsuzawa, and K. Tsuchiya, *J. Metastable Nanocryst. Mater.* 8, 918 (2000).
81. M. Zebarjadi, K. Esfarjani, A. Shakouri, J.-H. Bahk, Z. Bian, G. Zeng, J. Bowers, H. Lu, J. Zide, and A. Gossard, *Appl. Phys. Lett.* 94, 202105 (2009).
82. M.S. Dresselhaus, G. Chen, M.Y. Tang, R.G. Yang, H. Lee, D.Z. Wang, Z.F. Ren, J.-P. Fleurial, and P. Gogna, *Adv. Mater.* 19, 1043 (2007).
83. S.V. Faleev and F. Léonard, *Phys. Rev. B* 77, 214304 (2008).
84. S. Fiameni, S. Battiston, S. Boldrini, A. Famengo, F. Agresti, S. Barison, and M. Fabrizio, *J. Solid State Chem.* 193, 142 (2012).
85. T. Yi, S. Chen, S. Li, H. Yang, S. Bux, Z. Bian, N.A. Katcho, A. Shakouri, N. Mingo, J.-P. Fleurial, N.D. Browning, and S.M. Kauzlarich, *J. Mater. Chem.* 22, 24805 (2012).
86. N. Farahi, S. Prabhudev, M. Bugnet, G. Botton, J. Zhao, J.S. Tse, J.R. Salvador, and H. Kleinke, *RSC Adv.* 5, 65328 (2015).
87. A.S. Tazebay, S.-I. Yi, J.K. Lee, H. Kim, J.-H. Bahk, S.L. Kim, S.-D. Park, H.S. Lee, A. Shakouri, and C. Yu, *ACS Appl. Mater. Interfaces* 8, 7003 (2016).